

Ab Initio Modeling of Thermal Transport through van der Waals Materials

Sara Fiore* and Mathieu Luisier

Integrated Systems Laboratory, ETH Zurich, 8092 Zurich, Switzerland

An advanced modeling approach is presented to shed light on the thermal transport properties of van der Waals materials (vdWMs) composed of single-layer transition metal dichalcogenides (TMDs) stacked on top of each other with a total or partial overlap only in the middle region. It relies on the calculation of dynamical matrices from first-principle and on their usage in a phonon quantum transport simulator. We observe that vibrations are transferred microscopically from one layer to the other along the overlap region which acts as a filter selecting out the states that can pass through it. Our work emphasizes the possibility of engineering heat flows at the nanoscale by carefully selecting the TMD monolayers that compose vdWMs.

I. INTRODUCTION

During the last 50 years electronic devices have undergone a constant miniaturization of their dimensions following Moore's scaling law [1]. While the integration of always smaller components has paved the way for enhanced functionalities, several obstacles have recently emerged that could compromise the benefit of further size reductions [2]. In particular, modern transistors already operate at length scale of the same order as the electron and phonon mean free paths [3] where discrete scattering events and geometrical variations have a profound impact on their behaviour. The increased power density of these devices combined with high thermal dissipation and dramatic peak temperatures, severely limit their reliability, performance and lifetime [4],[5]. Another critical issue is self- or Joule-heating, a phenomenon caused by the phonon emission of high energy electrons [6]. Instead of eliminating thermal fluctuations several research efforts have tried to take advantage of nanoscale systems to recycle the waste heat through Seebeck's effect [7],[8]. Designing such thermoelectric devices or next-generation logic switch will only be possible if both their electronic and thermal properties are kept under control and their interactions well understood. Physics-based materials and device modeling can be of great help for that purpose, especially if combined with experiments in an holistic way. So far, the focus has been mainly set on the electronic characteristics of nanostructures [9],[10],[11],[12],[13],[14],[15],[16],[17] and much less on their thermal behaviour [18],[19],[20],[21].

To fill this gap and gain insight into nanoscale thermal management, we propose an original approach to model thermal transport and apply it to artificial materials called van der Waals Materials (vdWMs). Due to their ultimate thickness, van der Waals inter-layer coupling, intra-layer covalent bonds and surface free of dangling bonds, these compounds are expected to exhibit unique features [22],[23],[24],[25]. Since the breakthrough exfoliation of graphene in 2004 [26],[27] more than 1800 layered materials have been predicted to exist and some

of them have already been intensively investigated [28],[29]. In the 3D parents of 2D materials, strong covalent bonds hold together the crystalline structure in the in-plane direction, while van der Waals forces act along the out-of-plane axis connecting different layers. Hence, monolayers and few layers structures can be isolated and/or stacked on top of each other to form carefully designed van der Waals materials. Each 2-D material can be considered as a Lego brick that can be assembled with other building blocks. Several studies have been carried out on vdWMs, highlighting their potential as active region of future electronic (vertical field-effect transistors [30] and P-N diodes [31]), spintronic (magnetic tunneling junction [32] and spin field-effect transistors [33]) as well as optoelectronic (photodiodes [34] and photovoltaic detectors [35]) applications. The properties of vdWMs often go beyond the sum of the characteristics coming from each individual 2-D material composing them, such as unique band alignments [36] [37], fast charge transport [38][39], massive Dirac fermions [40][41], Hofstadter butterfly [42] and formation of interlayer excitons [43] [44] [45]. Furthermore, the behaviour of vdWMs can be tuned by playing with their geometry, for example the number of layers, twisting angles between different layers, or overlap lengths [46],[47]. Among the various types of vdWMs, we here consider those made of transition metal dichalcogenides (TMD).

All TMDs have a hexagonal crystalline structure made of three layers $X - M - X$, where X is a chalcogenide and M a transition metal. While their electrical properties have been explored extensively, both theoretically and experimentally [19],[48],[49],[50],[51], their thermal behavior has received much less attention although it could severely impact the applicability of these 2-D materials. For example, it has been shown that the thermal conductivity of TMDs is relatively low, about 2-3 orders of magnitude smaller than in graphene [52],[53],[54],[55],[56]. Consequently, large Joule heating effects and the formation of local hot spots have been observed in TMDs [57],[58],[59], which deteriorates the performance of devices made of such materials. Another important feature of vdWMs, is their highly anisotropic structure. The thermal conductivity of vdWMs strongly depends on the direction of propagation due to the

* Corresponding author: safiore@iis.ee.ethz.ch

weak van der Waals coupling that limits the heat flow along the out-of-plane axis [60],[61]. This property might allow vdWMs to operate as directional heat spreaders, dissipating heat more efficiently along a preferred direction [62]. Comparing theoretical results to experimental measurements represents a challenge for layered materials as building high-quality TMDs is a rather difficult process [63]. This typically leads to the presence of multiple defects such as stacking errors or layer spacing variations, which induce large uncertainties in the measurement of their properties. The thermal conductivity of MoS₂ can vary over one order of magnitude, over several orders of magnitudes for WSe₂ [64]. Another limitation comes from the determination of the proper thermal transport regime, often midway between the ballistic and diffusive cases. The lack of satisfactory agreement with experimental data suggests that other transport regimes might even be at play [65],[66]. In this paper, we investigate thermal transport through device configurations where the two TMD monolayers are stacked on top of each, either over the entire structure or only in their central part, as shown in Fig. 1. The electronic properties of such components have been investigated both theoretically [67] and experimentally [68],[69]: it has been shown that they can be used as active region of band-to-band tunneling field-effect transistors with potentially a steep subthreshold swing and a high ON-state current. This aspect is therefore ignored in the present study.

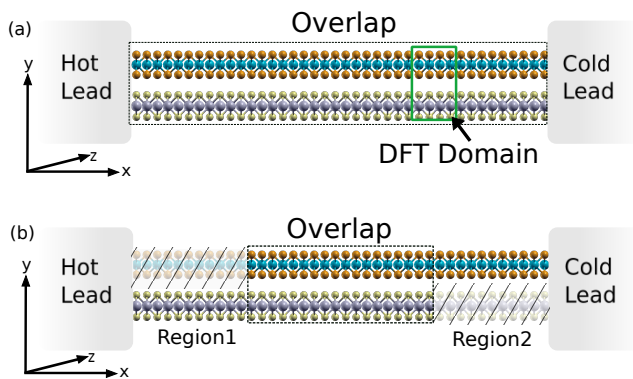


FIG. 1. (a) vdWM made of two TMDs with complete overlap. Such structures are referred to as TO channels. (b) Same as (a), but with a partial overlap of both TMDs in the middle and two regions made of single TMDs. Such structures are referred to as PO channels.

By applying a temperature gradient between both extremities of the structure with total (TO) and partial (PO) overlap in Fig. 1, phonons start propagating from the hot to the cold side. To model this phenomena, we restrict ourselves to ballistic thermal quantum transport (QT) simulations through vdWMs. The required dynamical matrices are first computed via density func-

tional perturbation theory (DFPT) and then passed to a QT solver relying on the Wave Function (WF) or Non-equilibrium Green's Function (NEGF) formalism to perform all thermal transport calculations. The present study intends to lay the foundations for future in-depth analyses involving more realistic effects such as anharmonic phonon decay or electron-phonon coupling.

The paper is organized as follows: in Section II an overview of the thermal transport equations is provided. Section III is dedicated to the calculation of dynamical matrices from first-principles. The influence of the inter-layer coupling is investigated in Section IV. Finally, in Section V thermal transport simulation results are presented for selected vdWMs with a partial overlap in the middle region and with total overlap. Conclusions are drawn in Section VI.

II. THERMAL TRANSPORT MODEL

Thermal transport is solved with a ballistic phonon quantum transport simulator based on the Wave Function (WF) or equivalently Non-equilibrium Green's Function (NEGF) formalism. In the WF formalism, the equations take the form of a sparse linear system of equations "Ax = b"

$$\left(\omega^2 \mathbb{1} - \Phi - \Pi^{RB}\right)\varphi = \text{Inj}, \quad (1)$$

which is numerically more efficient to handle than the NEGF equations in multi-dimensional structures.

In Eq. (1), Π^{RB} and Inj are the retarded boundary self-energy and the Injection vector, respectively. These terms describe the phonon injection into the simulation domain through open boundary conditions. They can be determined as described in Ref.[70]. The vector φ contains the crystal vibrations along all Cartesian coordinates. It is of size $3Na \times N_M$, where Na is the number of atoms in the system, whereas the number of columns N_M indicates that N_M states can be injected either from the left or the right contact at a given frequency ω . Finally, Φ is the dynamical matrix of the device of size $3Na \times 3Na$. A detailed description of its construction is given in Appendix A. All quantities (Π^{RB} , Φ , Inj and φ) depend on the phonon frequency and on the momentum q_z , which, for 2-D materials, is used to model the periodic, out-of-plane direction (z axis in Fig. 1). The knowledge of φ allows to compute the frequency- and momentum-dependent transmission function $\mathcal{T}(\hbar\omega, q_z)$, from which the thermal current I_{Th} can be evaluated based on the Landauer-Büttiker formalism [71],[72]

$$I_{Th} = \sum_{q_z} \frac{1}{N_{q_z}} \int \frac{d\omega}{2\pi} \mathcal{T}(\hbar\omega, q_z) \hbar\omega \left(b(\hbar\omega, T_L) - b(\hbar\omega, T_R) \right), \quad (2)$$

where N_{q_z} is the number of q_z points used to sample the periodic direction z and $b(\hbar\omega, T_{L(R)})$ is the Bose-Einstein

distribution function of the left (right) contact at temperature $T_{L(R)}$.

III. DFT SIMULATIONS

When simulating a vdWM the first step consists of constructing a suitable atomic structure, which might require assembling two planar materials with different unit cells and/or lattice constants. Symmetry considerations play a determinant role in this regard. Stacking MoS₂ and h-BN, for example, relies on a common hexagonal cell of at least 26 atoms due to the large lattice mismatch between both materials (h-BN: 2.51 Å, MoS₂: 3.18 Å). Here, to limit the computational burden, we only investigated possible combinations of three chalcogenides (S, Se, Te) and two transition metals (Mo, W) with 2H lattice. Hence, WTe₂ is discarded as it is only stable in its 1T' (metallic) form. The combinations MoTe₂-MoS(Se)₂ are not considered either because of the large lattice mismatch between them. Combining them would require either a unit cell with a large number of atoms or with a very high strain. Overall, 5 homobilayers (MoS₂-MoS₂, MoSe₂-MoSe₂, WS₂-WS₂, WSe₂-WSe₂ and MoTe₂-MoTe₂) and 6 hetero-bilayers (MoS₂-WS₂, MoS₂-WSe₂, MoS₂-MoSe₂, MoSe₂-WS₂, MoSe₂-WSe₂ and WS₂-WSe₂) are analyzed. The chosen stacking order to build them is AA' (D3d group), following the same notation as in Ref.[73]. The transition metal of

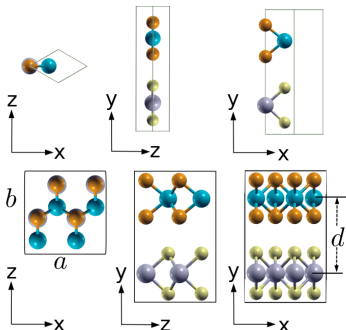


FIG. 2. Bilayer hexagonal (*top* panel) and orthorhombic (*bottom* panel) unit cell used for transport calculation viewed under different angles. Yellow (*orange*) spheres represent the chalcogenide atoms in the *bottom* (*top*) layer, violet (*turquoise*) spheres the transition metal atoms in the *bottom* (*top*) layer.

one layer is positioned over the chalcogenide of the other one. This mutual arrangement has been proved to be the one with lowest energy [73],[74],[75],[76]. Along the c -axis (stacking direction, aligned with the y -axis), a vacuum region of at least 20 Å is placed, to decouple periodic images and avoid spurious dipole interactions [77],[78]. Given the extreme similarity between the TMDs under investigation, the unit cells of the bilayers is directly obtained from the unit cell of the parent materials, without the

Lattice Vectors & Interlayer Distance (Å)			
Bilayer	a	b	d
MoS ₂ -MoS ₂	6.3786	5.5240	6.225
WS ₂ -WS ₂	6.3648	5.5121	6.090
WSe ₂ -WSe ₂	6.6352	5.7462	6.502
MoTe ₂ -MoTe ₂	7.1000	6.1488	6.977
MoSe ₂ -MoSe ₂	6.6368	5.7476	6.519
MoS ₂ -MoSe ₂	6.4784	5.6105	6.380
MoS ₂ -WS ₂	6.3753	5.5212	6.153
MoS ₂ -WSe ₂	6.5006	5.6297	6.320
MoSe ₂ -WS ₂	6.5008	5.6299	6.307
MoSe ₂ -WSe ₂	6.6360	5.7469	6.475
WS ₂ -WSe ₂	6.5000	5.6292	6.253

TABLE I. Orthorhombic unit cell dimensions of the investigated vdWMs where a and b refer to the in-plane axis, aligned with the x - and z -axis, respectively. The variable d indicates the distance along the y -axis between chalcogenides belonging to different layers, as depicted in Fig. 2

need to introduce a supercell. Indeed, with different symmetry the lattice constant of the bilayers is found to be very close to the one of the TMDs. The weak inter-layer interactions between the different 2-D materials induce a very small displacement of the atomic positions with respect to the isolated TMDs. The largest displacement we calculated was along the c -axis and in the order of 10^{-2} Å. The hexagonal unit cell of all considered TMDs is made of 3 atoms, so that, the hexagonal unit cell of the bilayers contains 6 atoms, as illustrated in the top panel of Fig. 2. Within the hexagonal cell of the bilayer, the atomic positions are accurately relaxed in order to avoid negative frequencies in the phonon spectrum. The convergence criteria was set to 10^{-8} Å/eV for the force acting on each ion. The generalized gradient approximation (GGA) of Perdew, Burke, and Ernzerhof (PBE) [79] was used as the exchange-correlation functional, while the van der Waals forces were included through the DFT-D2 parametrization of Grimme [80]. The plane-wave cutoff energy was set to 550 eV. Subsequently, the hexagonal cell is transformed into an orthorhombic cell, which is more convenient to perform quantum transport calculations. Such unit cells include 24 atoms, where 12 belong to one TMD and 12 to the other, as indicated in the bottom panel of Fig. 2. The lattice vectors and the interlayer distance of the orthorhombic cells are reported in Table I for all investigated configurations. A $2 \times 1 \times 2$ supercell discretized on a $3 \times 1 \times 3$ phonon wavevector grid was used to compute the real space force constants with the finite displacement method.

All DFT calculations were carried out with the Vienna *Ab initio* Software Package (VASP) [81],[82] and PHONOPY [83]. All inter-atomic interactions were cut

off beyond a radius $r_{cut} = 6.8\text{\AA}$ in the simulated vdWMs. It has been verified that this truncation does not affect the phonon bandstructure by more than 10%, ensuring accurate quantum transport calculations. As an example the dispersion of MoS₂-MoS₂ homo-bilayer is reported in Fig. 3 with the full and truncated interaction range. An excellent agreement can be observed between both sets of curves.

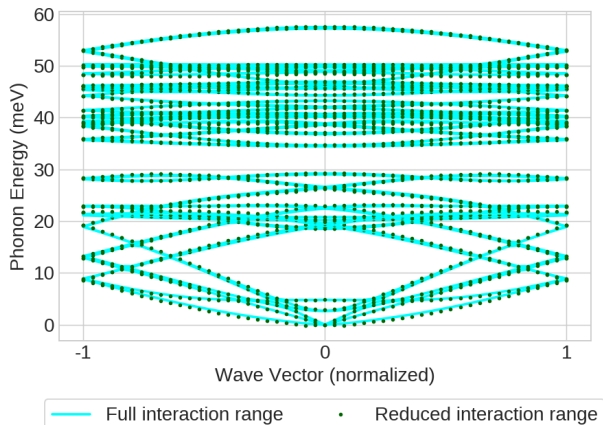


FIG. 3. Phonon dispersion of a MoS₂-MoS₂ homo-bilayer computed with PHONOPY [83] keeping the full inter-atomic interaction range (cyan lines) or truncating it beyond $r_{cut} = 6.8\text{\AA}$ (green dots).

IV. EFFECT OF THE INTER-LAYER COUPLING

Next, the impact of the inter-layer coupling (van der Waals forces) on the Interatomic Force Constants and phonon properties is studied. In Fig. 4(a) the schemat-

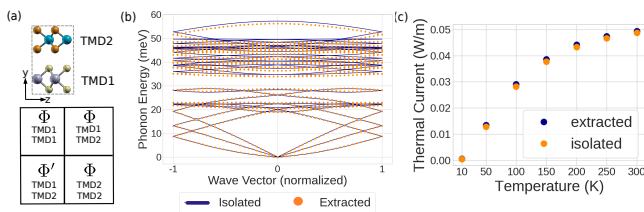


FIG. 4. (a) Bilayer structure made of TMD1 and TMD2 and corresponding schematics of the Interatomic Force Constants. (b) Phonon dispersion of monolayer MoS₂ computed from an isolated structure (blue lines) and when the dynamical matrix is extracted from MoS₂-WS₂ hetero-bilayer (orange dots). (c) Ballistic thermal current flowing through a MoS₂ monolayer calculated with the phonon dispersions from (b) as a function of the temperature. A thermal gradient $\Delta T = 0.1\text{ K}$ is applied between both extremities of the structure.

ics a vdWM bilayer is shown together with the corresponding dynamical matrix. The diagonal blocks contain the intra-layer interactions and the off diagonal

blocks the inter-layer coupling elements. The average magnitude of the intra-layer blocks ($\Phi_{\text{TMD1-TMD1}}$ and $\Phi_{\text{TMD2-TMD2}}$) entries exceeds that of the inter-layer blocks by a factor 500. Motivated by this observation we examined whether the properties of each individual layer could be retrieved from those of the stack. In other words, we wanted to verify whether the intra-layer matrices $\Phi_{\text{TMD1-TMD1}}$ ($\Phi_{\text{TMD2-TMD2}}$) in Fig. 4(a) could accurately describe the phonon dispersion and the ballistic thermal current flowing through a monolayer of TMD1(TMD2). To compute the ballistic thermal current a gradient $\Delta T = 0.1\text{ K}$ was applied between the temperature of the left (T_L) and the right (T_R) contacts, while varying T_L between 10 and 300 K. The phonon transport equations were solved by discretizing the periodic direction z with $N_{qz} = 51$ momentum points and by considering $N_M = 150$ frequency points. As an example, a MoS₂-WS₂ vdWM was chosen. The phonon bandstructure and thermal current of a MoS₂ monolayer were extracted and compared to data directly obtained from a calculation involving individual, isolated layer calculation. The results are reported in Fig. 4(b) and Fig. 4(c), respectively. The same type experiment was repeated for other 2-D material combinations: in all cases, the error between the data derived from the vdWM dynamical matrix and from a true monolayer remains below 10%. We continued our analysis with the thermal current flowing through vdWM bilayers overlapping over their entire surface, as in Fig. 1(a), and through the individual 2-D monolayer constituting them. For brevity, such bilayer structures with fully overlapping monolayers are referred to TO, while the isolated layers are labeled 1 and 2, where 1(2) indicate the first(second) TMD in the vdWM. The resulting bilayer is of the form $M^{(1)}X_2^{(1)} - M^{(2)}X_2^{(2)}$. All calculations were performed at 300 K with 1 K temperature difference between the left and right contact. Hence, $I_{Th,TO}$ is the current flowing through the TO structure, and $I_{Th,1(2)}$ through first(second) monolayers. We found that the relative error between $I_{Th,1} + I_{Th,2}$ and $I_{Th,TO}$ does not exceed 10%, as can be seen in Table II.

V. TRANSPORT SIMULATIONS AND RESULTS

In this Section, the ballistic thermal transport properties of vdWMs with partial overlap (as in Fig. 1(b)) are reported and analysed. The developed methodology allows to simulate such device configurations that are more complex and potentially more interesting than TO channels, where the two TMD monolayers are stacked on top of each other over their entire surface. In geometries with a partial TMD overlap, three distinct regions can be identified: one with an isolated monolayer TMD1, on the left, one with an isolated monolayer TMD2 on the right and one with a bilayer vdWM TMD1+TMD2 in the middle, as sketched in Fig. 1(b). In fact, the structure in Fig. 1(b) is obtained by removing atoms from the bilayer

Thermal Current [W/m]					
Bilayer	$I_{Th,1}$	$I_{Th,2}$	$I_{Th,TO}$	$I_{Th,1}$ + $I_{Th,2}$	Error [%]
MoS ₂ -MoS ₂	0.50037	0.50037	0.9855	1.0007	2
WS ₂ -WS ₂	0.3986	0.3986	0.7771	0.7972	3
WSe ₂ -WSe ₂	0.3166	0.3166	0.6145	0.6332	2
MoTe ₂ -MoTe ₂	0.2567	0.2567	0.4839	0.5134	6
MoSe ₂ -MoSe ₂	0.3472	0.3472	0.6676	0.6944	4
MoS ₂ -MoSe ₂	0.4994	0.3802	0.863	0.8796	2
MoS ₂ -WS ₂	0.4982	0.3762	0.8222	0.8744	6
MoS ₂ -WSe ₂	0.4812	0.3275	0.7417	0.8087	8
MoSe ₂ -WS ₂	0.3789	0.3821	0.7393	0.7610	3
MoSe ₂ -WSe ₂	0.3681	0.3132	0.6589	0.6813	3
WS ₂ -WSe ₂	0.3817	0.3359	0.6924	0.7176	4

TABLE II. Comparison between the thermal current flowing through 2-D individual monolayers ($I_{Th,1(2)}$) and through vdWM bilayers overlapping over the entire surface ($I_{Th,TO}$). The last column reports the relative error between $I_{Th,1} + I_{Th,2}$ and $I_{Th,TO}$

in Fig. 1(a) and by eliminating the corresponding entries from the dynamical matrix. A detailed description of the construction procedure and of the assembling of its device dynamical matrix is given in Appendix B. While it was demonstrated in the previous Section that the interlayer coupling has a limited influence on the thermal current flowing through a vdWM with a TO structure, the situation is radically different in the case of a partial overlap, even if the two layers are identical. In geometries similar to the one shown in Fig. 1(b), without inter-layer coupling, there would be no thermal current, thus making the van der Waals interactions a critical component of the heat flow. At the microscopic level, the different configuration of the three device regions forces the phonons to be transferred from one layer to the other. This does not prevent the application of our approach as the inter-layer coupling is fully captured in the overlap region, which ensures an accurate description of thermal transport there. As will be shown in the following, the thermal transport properties of a bilayer channel with a partial overlap cannot be predicted from the phonon bandstructure of the individual monolayers that compose it, contrary to structures where the TMDs are stacked over their entire surface. Atomistic quantum transport simulations are required to reveal their behaviour.

As starting point, the impact of the overlap length on the ballistic current is presented in Fig. 5, the goal being to study how this parameter affects the current magnitude and whether representative features can be identified. A slight dependence of the current on the overlap length can be observed in some of the homo-bilayers (both TMDs are identical). Below 100-150 Å, the thermal current linearly increase with the overlap length before saturating. This seems to indicate that a minimum overlap length is needed so that all phonon modes can

be transferred from one layer to the other. Note that very short overlap lengths are probably very challenging to achieve experimentally [84] and therefore practically of limited relevance. Hence, from now on, we restrict our investigations to devices with an overlap length of approximately 300 Å. With such dimensions, for all bilayers the simulation results are independent from the length of the overlap region. For brevity, we refer to bilayer structures with 300 Å of overlap as PO.

Table III reports three relevant quantities concerning the current flowing through these structures: (i) the ratio between $I_{th,PO}$ and $I_{th,TO}$, (ii) that between $I_{th,PO}$ and $I_{th,1}$ and (iii) that between $I_{th,PO}$ and $I_{th,2}$. Together with Fig. 5, these results highlight that the ballistic thermal current flowing through a PO channel is reduced by about 70% as compared to TO channel in case of homo-bilayers (MoS₂-MoS₂, MoSe₂-MoSe₂, WS₂-WS₂, WSe₂-WSe₂, MoTe₂-MoTe₂). A more significant decrease of approximately 95% is observed for hetero-bilayers (MoS₂-WS₂, MoS₂-WSe₂, MoS₂-MoSe₂, MoSe₂-WS₂, MoSe₂-WSe₂, WS₂-WSe₂). Perhaps even more important, the thermal current through PO structures is smaller than that flowing through either of the monolayers constituting it, by 40% for the homo-bilayers, much more for the hetero-bilayers.

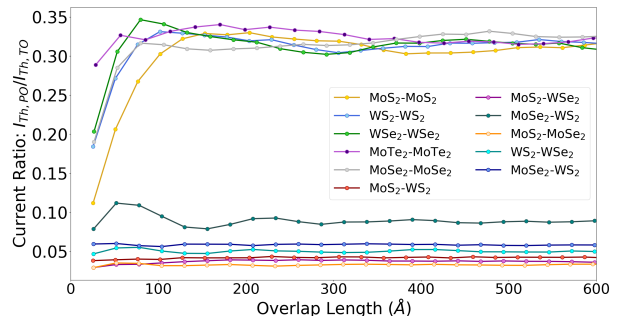


FIG. 5. Ballistic thermal current ratio $I_{Th,PO}/I_{Th,TO}$ for all the homo- and hetero-bilayer vdWMs considered in this work.

The extremely high thermal current reduction in case of hetero-bilayers can be attributed to the fact that in the ballistic limit of transport only states existing throughout the whole structure can be transmitted from one contact to the other [85]. This can be qualitatively explained by inspecting the phonon bandstructure and the vibrational density-of-states (VDOS) of the two TMDs composing the vdWM. As an example, in Fig. 6, the data for a MoS₂-WSe₂ hetero-bilayer is presented. While MoS₂ exhibits a mini-gap around the phonon energy $\hbar\omega = 30 meV$ ($27 < \hbar\omega < 32 meV$) and its energy range goes up to $\hbar\omega_{MAX} = 57 meV$, it can be seen that the energy window without VDOS for WSe₂ is different, i.e. $17 < \hbar\omega < 20 meV$, as well as its maximum energy ($\hbar\omega_{MAX} = 38 meV$). As a consequence, a phonon with energy $\hbar\omega = 45 meV$ injected from MoS₂ will not be able

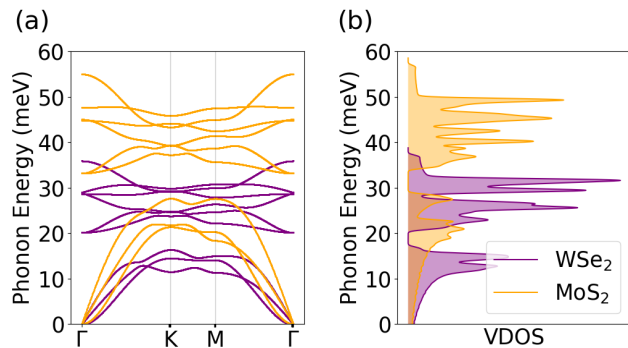


FIG. 6. (a) Phonon dispersion of MoS₂ (orange) and WSe₂ (purple) monolayers. (b) Corresponding Vibrational Density-of-States (VDOS).

Thermal Current			
Bilayer	$I_{Th,PO}/I_{Th,TO}$	$I_{Th,PO}/I_{Th,1}$	$I_{Th,PO}/I_{Th,2}$
MoS ₂ -MoS ₂	0.3147	0.6199	0.6199
WS ₂ -WS ₂	0.3070	0.5986	0.5986
WSe ₂ -WSe ₂	0.3115	0.6045	0.6045
MoTe ₂ -MoTe ₂	0.3224	0.6077	0.6077
MoSe ₂ -MoSe ₂	0.3168	0.6092	0.6092
MoS ₂ -MoSe ₂	0.0335	0.0579	0.0760
MoS ₂ -WS ₂	0.0429	0.0708	0.0937
MoS ₂ -WSe ₂	0.0386	0.0595	0.0874
MoSe ₂ -WS ₂	0.0877	0.1710	0.1696
MoSe ₂ -WSe ₂	0.0596	0.1068	0.1255
WS ₂ -WSe ₂	0.0487	0.0883	0.1003

TABLE III. Ratio between the ballistic thermal current flowing through the PO ($I_{th,PO}$) and TO ($I_{th,TO}$) structures and through the PO vdWMs and the isolated monolayers ($I_{th,1(2)}$) they are made of.

to be transferred to the WSe₂ monolayer, which reduces the number of states available for transport and the resulting thermal current. Further comparisons similar to Fig. 6 are provided in the Supplementary Materials, for other 2-D material combinations.

To continue our analysis, we examined on the energy (frequency) dependence of the thermal current. Fig. 7 shows the values of the cumulative ballistic thermal current $I_{Th}(\bar{\omega})$ of the homo-bilayer MoS₂-MoS₂ and the hetero-bilayer MoS₂-WSe₂ computed according to the following equation

$$I_{Th}(\bar{\omega}) = \frac{\sum_{q_z} \int_0^{\hbar\bar{\omega}} \frac{d\omega}{2\pi} \mathcal{T}(\hbar\omega, q_z) \hbar\omega \left(b(\hbar\omega, T_L) - b(\hbar\omega, T_R) \right)}{\sum_{q_z} \int_0^{\hbar\omega_{MAX}} \frac{d\omega}{2\pi} \mathcal{T}(\hbar\omega, q_z) \hbar\omega \left(b(\hbar\omega, T_L) - b(\hbar\omega, T_R) \right)}. \quad (3)$$

In Eq. (3) $\hbar\omega_{MAX}$ is the highest phonon energy of the

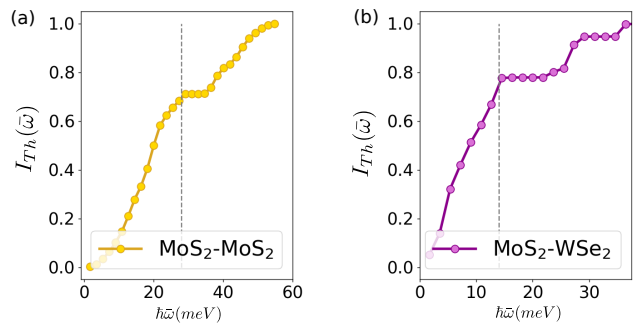


FIG. 7. (a) Cumulative ballistic thermal current of the homo-bilayer MoS₂-MoS₂ PO structure computed up the phonon energy $\hbar\bar{\omega}$, as described in Eq. (3). The dashed line indicates the end of the acoustic phonon branches of the TMD of the lower energy range. (b) Same as (a) but for the hetero-bilayer MoS₂-WSe₂ PO structures

vdWM. From this analysis it clearly appears that the major contribution to the ballistic thermal current comes from the acoustic branches. Similar analyses of all considered vdWMs with a PO configuration can be found in the Supplementary Materials.

As final step, we studied the energy distribution of the total transmission function $\mathcal{T}(\hbar\omega) = \frac{1}{N_{q_z}} \sum_{q_z} \mathcal{T}(\hbar\omega, q_z)$. To distinguish the different cases under investigation, we introduced the following notation: be $(n) \in \{\text{MoS}_2\text{-MoS}_2, \text{MoSe}_2\text{-MoSe}_2, \text{WS}_2\text{-WS}_2, \text{WSe}_2\text{-WSe}_2, \text{MoTe}_2\text{-MoTe}_2\}$ the index referring to the homo-bilayers, $(m) \in \{\text{MoS}_2\text{-WS}_2, \text{MoS}_2\text{-WSe}_2, \text{MoSe}_2\text{-MoSe}_2, \text{MoSe}_2\text{-WS}_2, \text{MoSe}_2\text{-WSe}_2, \text{WS}_2\text{-WSe}_2\}$ the index referring to the hetero-bilayers and $(C) \in \{\text{PO}, \text{TO}, 1, 2\}$ the index indicating the different channel configurations (partial overlap, total overlap, only first TMD, only second one). Fig. 8(a) reports the energy-resolved transmission functions $\mathcal{T}^{(n)(C)}(\hbar\omega)$ of the homo-bilayer $(n) = \text{MoS}_2\text{-MoS}_2$ with all possible channel configurations. Note that channels 1 and 2 are identical in this case. In Fig. 8(b), the comparison between $\mathcal{T}^{(n)(PO)}(\hbar\omega)$ and $\mathcal{T}^{(n)(TO)}(\hbar\omega)$ scaled by a factor 0.3, indicates that the energy profile of the transmission function in the PO channel can be obtained, as first approximation, by scaling the transmission function of the TO channel by a constant, energy-independent factor.

This behaviour can be interpreted by recalling the fact that in an homo-bilayer with a PO configuration, the initial and final states are the same. As they are mixed in the overlap region each state is degenerate. It should be emphasized that the scaling factor, 0.3, is in agreement with results of Table III and remains constants regardless of the TMD monolayers composing the homo-vdWMs (see the Supplementary Materials). Fig. 8(c) presents the same analysis as Fig. 8(a), but for the hetero-bilayer $(m) = \text{MoS}_2\text{-WSe}_2$ structure, where channels 1 and 2 differ. Contrary to the homo-bilayer case, the energy-resolved transmission function of PO configuration, $\mathcal{T}^{(m)(PO)}(\hbar\omega)$ cannot be obtained by

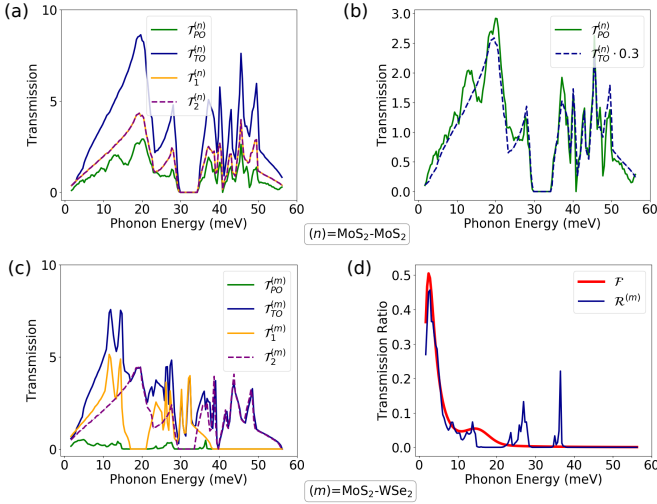


FIG. 8. (a) Transmission function $\mathcal{T}_C^{(n)}(\hbar\omega)$ of the homo-bilayer vdWM with $(n) = \text{MoS}_2\text{-MoS}_2$ case with different channel configuration $(C) = \text{PO}, \text{TO}, 1$ and 2 . (b) Comparison of $\mathcal{T}_{PO}^{(n)}(\hbar\omega)$ and $\mathcal{T}_{TO}^{(n)}(\hbar\omega)$ scaled by a factor 0.3 , for the homo-bilayer $(n) = \text{MoS}_2\text{-MoS}_2$ vdWM. (c) Same as (a), but for the hetero-bilayer vdWM with $(m) = \text{MoS}_2\text{-WSe}_2$ structure. (d) Transmission function ratio $\mathcal{R}^{(m)}(\hbar\omega) = \mathcal{T}_{PO}^{(m)}(\hbar\omega)/\mathcal{T}_{TO}^{(m)}(\hbar\omega)$ for the hetero-bilayer $(m) = \text{MoS}_2\text{-WSe}_2$ (blue line) and the function \mathcal{F} described by Eq. (6) (red line)

scaling $\mathcal{T}^{(m)(TO)}(\hbar\omega)$ or $\mathcal{T}^{(m)(1)}(\hbar\omega)$ and $\mathcal{T}^{(m)(2)}(\hbar\omega)$. Indeed, a combination of the transmission functions of the isolated monolayers would only account for the presence of mini-gaps as well as for the extension of the energy spectra already noticed in Fig. 6. By building the transmission function ratio

$$\mathcal{R}^{(m)}(\hbar\omega) = \frac{\mathcal{T}^{(m)(PO)}(\hbar\omega)}{\mathcal{T}^{(m)(TO)}(\hbar\omega)}, \quad (4)$$

which is reported in Fig. 8(d) for $\text{MoS}_2\text{-WSe}_2$, a peak can be detected at 5 meV , followed by bumps of much smaller intensity. We repeated the same calculation for all hetero-bilayers, as reported in the Supplementary Materials, we found that all $\mathcal{R}^{(m)}(\hbar\omega)$ exhibit a peak with a magnitude of about 0.5 , at approximately $\hbar\omega = 5 \text{ meV}$, followed by bumps, whose behaviour depends on the material combination. Based on this observation we computed the average transmission function ration

$$\mathcal{R}_{AVG}(\hbar\omega) = \frac{1}{N_m} \sum_m \mathcal{R}^{(m)}(\hbar\omega) \quad (5)$$

where $N_m = 6$ is the number of hetero-bilayers that we investigated. $\mathcal{R}_{AVG}(\hbar\omega)$ can be fitted using the expression:

$$\mathcal{F}(\hbar\omega) = \mathcal{L}(\hbar\omega, \mu_1, \eta, A) + \frac{1}{N} e^{-(\hbar\omega - \mu_2)/2\sigma^2}, \quad (6)$$

where \mathcal{L} is the Landau distribution function, as defined in Ref. [86], using the following parameters $(\mu_1, \eta, A, \mu_2, \sigma, N) = (1749.97, 549.68, 0.505, 15, 3, 0.04)$. The function $\mathcal{F}(\hbar\omega)$ is plotted in Fig. 8(d). As \mathcal{F} approximates the ratio between the $\mathcal{T}_{PO}^{(m)}(\hbar\omega)$ and $\mathcal{T}_{TO}^{(m)}(\hbar\omega)$, from the knowledge of $\mathcal{T}_{TO}^{(m)}(\hbar\omega)$, which can be derived from $\mathcal{T}_1^{(m)}(\hbar\omega)$ and $\mathcal{T}_2^{(m)}(\hbar\omega)$, we can estimate the thermal current flowing through a hetero-bilayer with a PO configuration

$$I_{\mathcal{F}}^{(m)} = \int_0^{\hbar\omega_{MAX}} \frac{d\omega}{2\pi} \mathcal{T}_{TO}^{(m)}(\hbar\omega) \mathcal{F}(\hbar\omega) \hbar\omega \cdot \left(b(\hbar\omega, T_L) - b(\hbar\omega, T_R) \right). \quad (7)$$

The ratio between $I_{\mathcal{F}}^{(m)}$ and the corresponding ballistic thermal current $I_{PO}^{(m)}$ obtained with a quantum transport simulation is listed in Table IV. It can be observed that the non-uniformly scaled transmission function $\mathcal{T}_{TO}^{(m)}(\hbar\omega) \mathcal{F}(\hbar\omega)$ of Eq. (7) can reproduce the quantum mechanical results with an error that does not exceed 35%. Only $\text{MoSe}_2\text{-WS}_2$ does not follow this trend, due to a large transmission contribution in the energy region $10 \leq \hbar\omega \leq 20 \text{ meV}$ which is not correctly captured by the function $\mathcal{F}(\hbar\omega)$. Still, it can be deduced that the hetero-vdWMs with a PO configuration mainly act as low-pass filter of the corresponding TO transmission function.

Thermal Current	
Hetero-Bilayer (m)	$I_{\mathcal{F}}^{(m)}/I_{PO}^{(m)}$
$\text{MoS}_2\text{-WS}_2$	0.65
$\text{MoS}_2\text{-WSe}_2$	0.83
$\text{MoSe}_2\text{-WS}_2$	0.37
$\text{MoS}_2\text{-MoSe}_2$	0.82
$\text{WS}_2\text{-WSe}_2$	0.73
$\text{MoSe}_2\text{-WSe}_2$	0.63

TABLE IV. Ratio between $I_{\mathcal{F}}^{(m)}$ and the corresponding ballistic thermal current $I_{PO}^{(m)}$ calculated with a quantum transport simulation for hetero-bilayer vdWMs with a PO configuration.

Besides the PO structure analyzed in this work, two other arrangements of vdWMs can be envisioned. The first possibility is illustrated in Fig. 9(a), where one TMD is extended along the whole device length, while the other covers only a part of the distance separating both electrodes. Such structures are referred to as 1O (2O) channels, if the TMD extended along the whole length is TMD1 (TMD2). In the second possibility, depicted in Fig. 9(b), one TMD extends along the whole structure, whereas the second one is only present in the central region and not connected to any lead. This configuration is labeled 1O1 (2O2) channels if the TMD extended

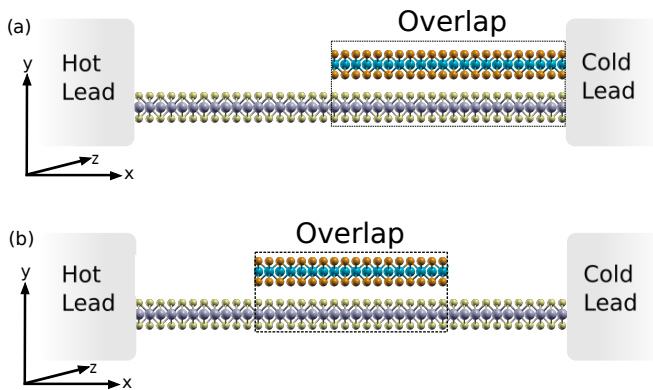


FIG. 9. (a) vdWM made of two TMDs, where one TMD extends over the whole device length, while the other goes from one reservoir to the middle of the device. Such structure is referred to as 1O(2O) if TMD1(TMD2) is connected to both reservoirs. (b) vdWM made of two TMDs, one covering the entire device length and the other only existing in the central region, without connection to the reservoirs. Such structures are labeled 1O1(2O2) if TMD1(TMD2) is extended over the whole length

Thermal Current [W/m]		
Bilayers	$I_{Th,1O}/I_{Th,1}$	$I_{Th,2O}/I_{Th,2}$
MoS ₂ -MoS ₂	0.95	0.95
WS ₂ -WS ₂	0.92	0.93
WSe ₂ -WSe ₂	0.92	0.92
MoTe ₂ -MoTe ₂	0.90	0.90
MoSe ₂ -MoSe ₂	0.97	0.97
MoS ₂ -MoSe ₂	0.93	0.94
MoS ₂ -WS ₂	0.92	0.91
MoS ₂ -WSe ₂	0.95	0.93
MoSe ₂ -WS ₂	0.93	0.90
MoSe ₂ -WSe ₂	0.94	0.89
WS ₂ -WSe ₂	0.88	0.90

TABLE V. Ratio between the ballistic thermal current flowing through the 1O ($I_{th,1O}$) structure and TMD1 ($I_{th,1}$) and through the 2O ($I_{th,2O}$) ones and TMD2 ($I_{th,2}$)

along the whole length is TMD1 (TMD2). The ratio between the ballistic thermal current flowing through the 1O ($I_{th,1O}$) structure and TMD1 ($I_{th,1}$) and through the 2O ($I_{th,2O}$) structure and TMD2 ($I_{th,2}$) are presented in Table V. The latter shows that 1O (2O) devices behave as the TMD extended over the whole length. Table VI reports the ratio between the ballistic thermal current flowing through the 1O1 structure ($I_{th,1O1}$) and TMD1 ($I_{th,1}$) as well as through the 2O2 structure ($I_{th,2O2}$) and TMD2 ($I_{th,2}$). In the homo-bilayer cases, both the 1O1 and 2O2 configurations allow for a similar percentage of the thermal current to flow through them (with respect to $I_{th,1}$ and $I_{th,2}$) as the comparable PO structures, about 60%. The situation is different in the hetero-bilayer de-

Thermal Current [W/m]		
Bilayers	$I_{Th,1O1}/I_{Th,1}$	$I_{Th,2O2}/I_{Th,2}$
MoS ₂ -MoS ₂	0.57	0.57
WS ₂ -WS ₂	0.58	0.58
WSe ₂ -WSe ₂	0.59	0.59
MoTe ₂ -MoTe ₂	0.59	0.59
MoSe ₂ -MoSe ₂	0.58	0.58
MoS ₂ -MoSe ₂	0.90	0.91
MoS ₂ -WS ₂	0.90	0.93
MoS ₂ -WSe ₂	0.92	0.88
MoSe ₂ -WS ₂	0.86	0.83
MoSe ₂ -WSe ₂	0.86	0.85
WS ₂ -WSe ₂	0.83	0.86

TABLE VI. Ratio between the ballistic thermal current flowing through the 1O1 structure ($I_{th,1O1}$) and TMD1 ($I_{th,1}$) and through the 2O2 structure ($I_{th,2O2}$) and TMD2 ($I_{th,2}$).

vices where the thermal current is found to reach more than 80% of the value corresponding to the TMD connected to both contacts. The strength of the inter-layer coupling explains this behavior. Because these interactions are larger in homo-bilayer structures, the impact of stacking a disconnected TMD layer on top of a connected one is more pronounced there than in hetero-bilayers. More phonons are indeed transferred to the top layer, if it is the same as the bottom one. Parts of these phonons are transmitted back to the bottom layer, the rest is reflected back to its origin. Note that as for the PO configurations, the simulation results in Table VI do not depend on the length of the overlap region. This clearly indicates that stacking two TMD layers on top of each other, even if they weakly interact and a direct path exists between both electrodes, can have a profound impact on the thermal properties of such assemblies.

VI. CONCLUSIONS AND OUTLOOK

We explored the thermal transport properties of homo- and hetero-bilayer vdWMs made of two TMDs with total and partial overlap in the middle. To do that, we developed a suitable quantum transport approach where the simulation domain is created from structures with a full overlap of both TMDs and atoms are removed on both extremities, together with the corresponding entries of the dynamical matrix. We demonstrated that in structures with full TMD overlap the inter-layer interactions marginally contribute to the thermal current, while their existence is crucial to enable the transfer of phonons from one layer to the other in case of partial overlap. For large overlap lengths, we showed that the ballistic thermal current flowing through partially overlapping channels is insensitive to the variation of this parameter. Partial overlap systems act as filters that reduce the ballistic thermal current by approximately 70%

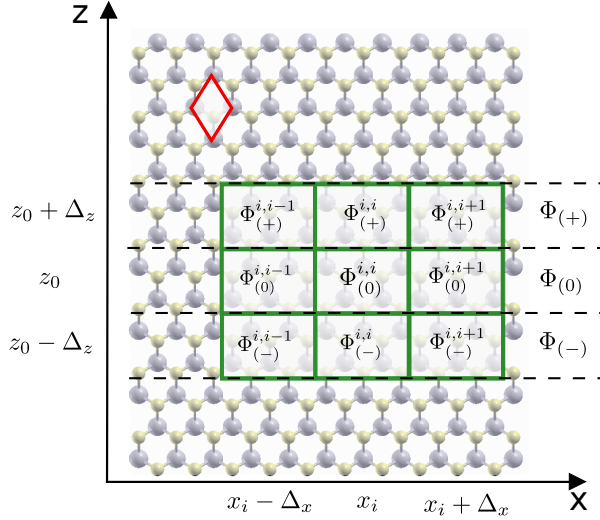


FIG. 10. Top view of a MoS₂ structure, where x denotes the transport direction, y the direction of confinement and z is assumed to be periodic and modeled through a set of q_z points. The dynamical matrices $\Phi(q_z)$ is computed by extracting all $\Phi_{(\alpha)}^{i,j}$ blocks required to construct the matrix of Eq. (A2). The red area marks the primitive hexagonal cell, while the green box the orthorhombic unit cells.

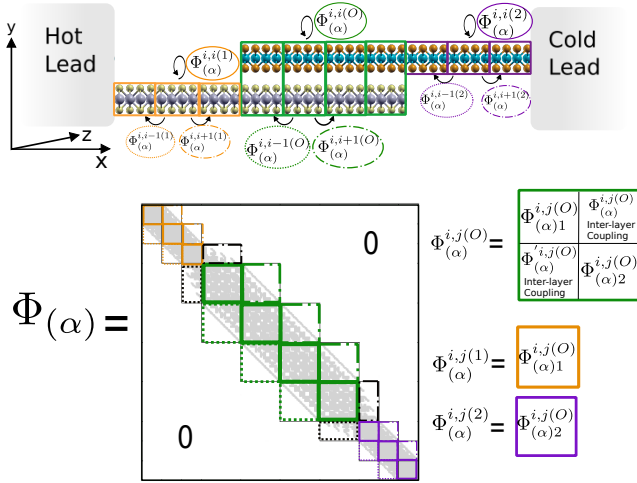


FIG. 11. (Top) Schematics of TMD monolayers stacked on top of each other with a partial overlap region in the middle. The on-site ($\Phi_{i,i}$) and nearest-neighbor ($\Phi_{i,i\pm 1}$) blocks of the dynamical matrix are indicated. (Bottom) Sparsity pattern of the corresponding device dynamical matrix. The blocks are colored according to their position in the device structure from the top panel.

green cell in the Overlap Region corresponds to the one of the total overlap case is the one that was used to compute the interatomic force constants with DFT. The orange(purple) cell contains only the bottom(top) TMD, the top(bottom) layer and the corresponding entries of the dynamical matrix having been removed. The validity

of this approach was demonstrated in Section IV, where it was shown that the inter-layer coupling does not strongly affect the properties of the individual layers. Concretely, in the overlap region, each $\Phi_{(\alpha)}^{i,j(O)}$ block is made of four sub-blocks, the diagonal ones connecting two unit cells of the same TMD with each other, the off-diagonal blocks coupling the two TMDs together. To construct the dynamical matrix of Region1(2), the diagonal blocks of $\Phi_{(\alpha)}^{i,j(O)}$ are extracted and labeled $\Phi_{(\alpha)}^{i,j(1)}$ ($\Phi_{(\alpha)}^{i,j(2)}$). The whole process is described in details in Fig. 11.

- [1] S. E. Thompson and S. Parthasarathy, "Moore's law: the future of si microelectronics," *Materials Today*, vol. 9, no. 6, pp. 20 – 25, 2006. [Online]. Available: <http://www.sciencedirect.com/science/article/pii/S1369702106715395>
- [2] P. Ball, "Computer engineering: Feeling the heat," *Nature News*, vol. 492, no. 7428, p. 174, 2012.
- [3] E. Pop and K. Goodson, "Thermal phenomena in nanoscale transistors," vol. 128, 07 2004, pp. 1– 7 Vol.1.
- [4] S. V. Garimella, A. S. Fleischer, J. Y. Murthy, A. Keshavarzi, R. Prasher, C. Patel, S. H. Bhavnani, R. Venkatasubramanian, R. Mahajan, Y. Joshi, B. Sammakia, B. A. Myers, L. Chorosinski, M. Baelmans, P. Sathyamurthy, and P. E. Raad, "Thermal challenges in next-generation electronic systems," *IEEE Transactions on Components and Packaging Technologies*, vol. 31, no. 4, pp. 801–815, Dec 2008.
- [5] E. Pop, S. Sinha, and K. E. Goodson, "Heat generation and transport in nanometer-scale transistors," *Proceedings of the IEEE*, vol. 94, no. 8, pp. 1587–1601, Aug 2006.
- [6] A. Sood, E. Pop, M. Asheghi, and K. E. Goodson, "The heat conduction renaissance," *2018 17th IEEE Intersociety Conference on Thermal and Thermomechanical Phenomena in Electronic Systems (ITherm)*, May 2018. [Online]. Available: <http://dx.doi.org/10.1109/ITHERM.2018.8419484>
- [7] R. Biele, C. A. Rodríguez-Rosario, T. Frauenheim, and A. Rubio, "Controlling heat and particle currents in nanodevices by quantum observation," *npj Quantum Materials*, vol. 2, no. 1, Jul 2017. [Online]. Available: <http://dx.doi.org/10.1038/s41535-017-0043-6>
- [8] R. He, G. Schierning, and K. Nielsch, "Thermoelectric devices: a review of devices, architectures, and contact optimization," *Advanced Materials Technologies*, vol. 3, no. 4, p. 1700256, 2018.
- [9] T. Mimura, S. Hiyamizu, T. Fujii, and K. Nanbu, "A new field-effect transistor with selectively doped gaas/n-alxgal-xas heterojunctions," *Japanese journal of applied physics*, vol. 19, no. 5, p. L225, 1980.
- [10] J. Faist, F. Capasso, D. L. Sivco, C. Sirtori, A. L. Hutchinson, and A. Y. Cho, "Quantum cascade laser," *Science*, vol. 264, no. 5158, pp. 553–556, 1994.
- [11] E. Yablonovitch, "Photonic band-gap crystals," *Journal of Physics: Condensed Matter*, vol. 5, no. 16, p. 2443, 1993.
- [12] X. Cheng, "10 - nanostructures: fabrication and applications," in *Nanolithography*, M. Feldman, Ed. Woodhead Publishing, 2014, pp. 348 – 375. [Online]. Available: <http://www.sciencedirect.com/science/article/pii/B9780857095008500105>
- [13] A. M. Ionescu and H. Riel, "Tunnel field-effect transistors as energy-efficient electronic switches," *nature*, vol. 479, no. 7373, pp. 329–337, 2011.
- [14] G. Dewey, B. Chu-Kung, J. Boardman, J. Fastenau, J. Kavalieros, R. Kotlyar, W. Liu, D. Lubyshev, M. Metz, N. Mukherjee *et al.*, "Fabrication, characterization, and physics of iii-v heterojunction tunneling field effect transistors (h-tfet) for steep sub-threshold swing," in *2011 International electron devices meeting*. IEEE, 2011, pp. 33–6.
- [15] R. K. Ghosh and S. Mahapatra, "Monolayer transition metal dichalcogenide channel-based tunnel transistor," *IEEE Journal of the electron devices society*, vol. 1, no. 10, pp. 175–180, 2013.
- [16] K.-T. Lam, X. Cao, and J. Guo, "Device performance of heterojunction tunneling field-effect transistors based on transition metal dichalcogenide monolayer," *IEEE electron device letters*, vol. 34, no. 10, pp. 1331–1333, 2013.
- [17] L. Britnell, R. Gorbachev, R. Jalil, B. Belle, F. Schedin, A. Mishchenko, T. Georgiou, M. Katsnelson, L. Eaves, S. Morozov *et al.*, "Field-effect tunneling transistor based on vertical graphene heterostructures," *Science*, vol. 335, no. 6071, pp. 947–950, 2012.
- [18] M. Maldovan, "Sound and heat revolutions in phononics," *Nature*, vol. 503, pp. 209–217, 2013.
- [19] S. Vaziri, E. Yalon, M. Muñoz Rojo, S. Suryavanshi, H. Zhang, C. McClellan, C. Bailey, K. Smithe, A. Gabourie, V. Chen, S. Deshmukh, L. Bendersky, A. Davydov, and E. Pop, "Ultrahigh thermal isolation across heterogeneously layered two-dimensional materials," *Science advances*, vol. 5, no. 8, 9 2019.
- [20] P. Rodgers, "Prediction of microelectronics thermal behavior in electronic equipment: status, challenges and future requirements," *Journal of microelectronics and electronic packaging*, vol. 1, no. 1, pp. 16–29, 2004.
- [21] C. Wan, X. Gu, F. Dang, T. Itoh, Y. Wang, H. Sasaki, M. Kondo, K. Koga, K. Yabuki, G. J. Snyder, R. Yang, and K. Koumoto, "Flexible n-type thermoelectric materials by organic intercalation of layered transition metal dichalcogenide tis₂," *Nature Materials*, vol. 14, 2015.
- [22] D. Akinwande, N. Petrone, and J. Hone, "Two-dimensional flexible nanoelectronics," *Nature communications*, vol. 5, no. 1, pp. 1–12, 2014.
- [23] M. Osada and T. Sasaki, "Exfoliated oxide nanosheets: new solution to nanoelectronics," *Journal of Materials Chemistry*, vol. 19, no. 17, pp. 2503–2511, 2009.
- [24] P. Miró, M. Audiffred, and T. Heine, "An atlas of two-dimensional materials," *Chemical Society Reviews*, vol. 43, no. 18, pp. 6537–6554, 2014.
- [25] P. Kumar, H. Abuhimd, W. Wahyudi, M. Li, J. Ming, and L.-J. Li, "Review—two-dimensional layered materials for energy storage applications," *ECS Journal of Solid State Science and Technology*, vol. 5, no. 11, pp. Q3021–Q3025, 2016.
- [26] K. S. Novoselov, "Electric field effect in atomically thin carbon films," *Science*, vol. 306, no. 5696, p. 666–669, Oct 2004. [Online]. Available: <http://dx.doi.org/10.1126/science.1102896>
- [27] K. S. Novoselov, A. K. Geim, S. V. Morozov, D. Jiang, M. I. Katsnelson, I. V. Grigorieva, S. V. Dubonos, and A. A. Firsov, "Two-dimensional gas of massless dirac fermions in graphene," *Nature*, vol. 438, no. 7065, p. 197–200, Nov 2005. [Online]. Available: <http://dx.doi.org/10.1038/nature04233>
- [28] M. Berger, *Nanoengineering: The Skills and Tools Making Technology Invisible*. Royal Society of Chemistry, 2019. [Online]. Available: <https://books.google.ch/books?id=HnB1xgEACAAJ>
- [29] N. Mounet, M. Gibertini, P. Schwaller, D. Campi, A. Merkys, A. Marrazzo, T. Sohier, I. E. Castelli, A. Ce-

- pellotti, and N. Pizzi, G. Marzari, “Two-dimensional materials from high-throughput computational exfoliation of experimentally known compounds, materials cloud archive,” 2019.
- [30] J. Wang, R. Jia, Q. Huang, C. Pan, J. Zhu, H. Wang, C. Chen, Y. Zhang, Y. Yang, H. Song *et al.*, “Vertical ws_2/sns_2 van der waals heterostructure for tunneling transistors,” *Scientific reports*, vol. 8, no. 1, pp. 1–9, 2018.
- [31] J. Y. Lim, M. Kim, Y. Jeong, K. R. Ko, S. Yu, H. G. Shin, J. Y. Moon, Y. J. Choi, Y. Yi, T. Kim *et al.*, “Van der waals junction field effect transistors with both n- and p-channel transition metal dichalcogenides,” *npj 2D Materials and Applications*, vol. 2, no. 1, pp. 1–7, 2018.
- [32] X. Li, J.-T. Lu, J. Zhang, L. You, Y. Su, and E. Y. Tsymbal, “Spin-dependent transport in van der waals magnetic tunnel junctions with fe_3gete_2 electrodes,” *Nano letters*, vol. 19, no. 8, pp. 5133–5139, 2019.
- [33] S. Jiang, L. Li, Z. Wang, J. Shan, and K. F. Mak, “Spin tunnel field-effect transistors based on two-dimensional van der waals heterostructures,” *Nature Electronics*, vol. 2, no. 4, pp. 159–163, 2019.
- [34] F. Wu, Q. Li, P. Wang, H. Xia, Z. Wang, Y. Wang, M. Luo, L. Chen, F. Chen, J. Miao *et al.*, “High efficiency and fast van der waals hetero-photodiodes with a unilateral depletion region,” *Nature communications*, vol. 10, no. 1, pp. 1–8, 2019.
- [35] Y. Chen, X. Wang, G. Wu, Z. Wang, H. Fang, T. Lin, S. Sun, H. Shen, W. Hu, J. Wang *et al.*, “High-performance photovoltaic detector based on $\text{mote}_2/\text{mos}_2$ van der waals heterostructure,” *Small*, vol. 14, no. 9, p. 1703293, 2018.
- [36] C. Gong, H. Zhang, W. Wang, L. Colombo, R. M. Wallace, and K. Cho, “Band alignment of two-dimensional transition metal dichalcogenides: Application in tunnel field effect transistors,” *Applied Physics Letters*, vol. 103, no. 5, p. 053513, 2013.
- [37] M.-H. Chiu, C. Zhang, H.-W. Shiu, C.-P. Chuu, C.-H. Chen, C.-Y. S. Chang, C.-H. Chen, M.-Y. Chou, C.-K. Shih, and L.-J. Li, “Determination of band alignment in the single-layer $\text{mos}_2/\text{wse}_2$ heterojunction,” *Nature communications*, vol. 6, no. 1, pp. 1–6, 2015.
- [38] F. Ceballos, M. Z. Bellus, H.-Y. Chiu, and H. Zhao, “Ultrafast charge separation and indirect exciton formation in a mos_2 – mose_2 van der waals heterostructure,” *ACS nano*, vol. 8, no. 12, pp. 12 717–12 724, 2014.
- [39] X. Hong, J. Kim, S.-F. Shi, Y. Zhang, C. Jin, Y. Sun, S. Tongay, J. Wu, Y. Zhang, and F. Wang, “Ultrafast charge transfer in atomically thin mos_2/ws_2 heterostructures,” *Nature nanotechnology*, vol. 9, no. 9, pp. 682–686, 2014.
- [40] L. Ponomarenko, R. Gorbachev, G. Yu, D. Elias, R. Jalil, A. Patel, A. Mishchenko, A. Mayorov, C. Woods, J. Wallbank *et al.*, “Cloning of dirac fermions in graphene superlattices,” *Nature*, vol. 497, no. 7451, pp. 594–597, 2013.
- [41] B. Hunt, J. D. Sanchez-Yamagishi, A. F. Young, M. Yankowitz, B. J. LeRoy, K. Watanabe, T. Taniguchi, P. Moon, M. Koshino, P. Jarillo-Herrero *et al.*, “Massive dirac fermions and hofstadter butterfly in a van der waals heterostructure,” *Science*, vol. 340, no. 6139, pp. 1427–1430, 2013.
- [42] C. R. Dean, L. Wang, P. Maher, C. Forsythe, F. Ghahari, Y. Gao, J. Katoch, M. Ishigami, P. Moon, M. Koshino *et al.*, “Hofstadter’s butterfly and the fractal quantum hall effect in moiré superlattices,” *Nature*, vol. 497, no. 7451, pp. 598–602, 2013.
- [43] P. Rivera, J. R. Schaibley, A. M. Jones, J. S. Ross, S. Wu, G. Aivazian, P. Klement, K. Seyler, G. Clark, N. J. Ghimire *et al.*, “Observation of long-lived interlayer excitons in monolayer mose_2 – wse_2 heterostructures,” *Nature communications*, vol. 6, no. 1, pp. 1–6, 2015.
- [44] Y. Yu, S. Hu, L. Su, L. Huang, Y. Liu, Z. Jin, A. A. Purezky, D. B. Geohegan, K. W. Kim, Y. Zhang *et al.*, “Efficient interlayer relaxation and transition of excitons in epitaxial and non-epitaxial mos_2/ws_2 heterostructures,” *arXiv preprint arXiv:1403.6181*, 2014.
- [45] H. Fang, C. Battaglia, C. Carraro, S. Nemsak, B. Ozdol, J. S. Kang, H. A. Bechtel, S. B. Desai, F. Kronast, A. A. Unal *et al.*, “Strong interlayer coupling in van der waals heterostructures built from single-layer chalcogenides,” *Proceedings of the National Academy of Sciences*, vol. 111, no. 17, pp. 6198–6202, 2014.
- [46] P. Ajayan, P. Kim, and K. Banerjee, “Two-dimensional van der waals materials,” *Physics Today*, vol. 69, no. 9, pp. 38–44, 2016. [Online]. Available: <https://doi.org/10.1063/PT.3.3297>
- [47] D. L. Duong, S. J. Yun, and Y. H. Lee, “van der waals layered materials: Opportunities and challenges,” *ACS Nano*, vol. 11, no. 12, pp. 11 803–11 830, 2017, pMID: 29219304. [Online]. Available: <https://doi.org/10.1021/acsnano.7b07436>
- [48] A. K. Geim and I. V. Grigorieva, “Van der waals heterostructures,” *Nature*, vol. 499, no. 7459, pp. 419–425, 2013.
- [49] R. Frisenda, E. Navarro-Moratalla, P. Gant, D. P. De Lara, P. Jarillo-Herrero, R. V. Gorbachev, and A. Castellanos-Gomez, “Recent progress in the assembly of nanodevices and van der waals heterostructures by deterministic placement of 2d materials,” *Chemical Society Reviews*, vol. 47, no. 1, pp. 53–68, 2018.
- [50] K. Novoselov, A. Mishchenko, A. Carvalho, and A. C. Neto, “2d materials and van der waals heterostructures,” *Science*, vol. 353, no. 6298, p. aac9439, 2016.
- [51] A. A. Balandin, “Thermal properties of graphene and nanostructured carbon materials,” *Nature materials*, vol. 10, no. 8, pp. 569–581, 2011.
- [52] W. Li, J. Carrete, and N. Mingo, “Thermal conductivity and phonon linewidths of monolayer mos_2 from first principles,” *Applied Physics Letters*, vol. 103, no. 25, p. 253103, 2013.
- [53] X. Liu and Y.-W. Zhang, “Thermal properties of transition-metal dichalcogenide,” *Chinese Physics B*, vol. 27, no. 3, p. 034402, mar 2018. [Online]. Available: <https://doi.org/10.1088%2F1674-1056%2F27%2F3%2F034402>
- [54] R. Yan, J. R. Simpson, S. Bertolazzi, J. Brivio, M. Watson, X. Wu, A. Kis, T. Luo, A. R. Hight Walker, and H. G. Xing, “Thermal conductivity of monolayer molybdenum disulfide obtained from temperature-dependent raman spectroscopy,” *ACS nano*, vol. 8, no. 1, pp. 986–993, 2014.
- [55] A. Taube, J. Judek, A. Lapinska, and M. Zdrojek, “Temperature-dependent thermal properties of supported mos_2 monolayers,” *ACS applied materials & interfaces*, vol. 7, no. 9, pp. 5061–5065, 2015.
- [56] G. Zhang and Y.-W. Zhang, “Thermoelectric properties of two-dimensional transition metal dichalcogenides,” *Journal of Materials Chemistry C*, vol. 5, no. 31, pp. 7684–7698, 2017.

- [57] E. Pop, "Energy dissipation and transport in nanoscale devices," *Nano Research*, vol. 3, no. 3, pp. 147–169, 2010.
- [58] Y. Fu, J. Hansson, Y. Liu, S. Chen, A. Zehri, M. K. Samani, N. Wang, Y. Ni, Y. Zhang, Z.-B. Zhang *et al.*, "Graphene related materials for thermal management," *2D Materials*, vol. 7, no. 1, p. 012001, 2019.
- [59] S. Sahoo, A. P. Gaur, M. Ahmadi, M. J.-F. Guinel, and R. S. Katiyar, "Temperature-dependent raman studies and thermal conductivity of few-layer mos₂," *The Journal of Physical Chemistry C*, vol. 117, no. 17, pp. 9042–9047, 2013.
- [60] H. Sadeghi, S. Sangtarash, and C. J. Lambert, "Cross-plane enhanced thermoelectricity and phonon suppression in graphene/mos₂ van der waals heterostructures," *2D Materials*, vol. 4, no. 1, p. 015012, 2016.
- [61] E. Pop, V. Varshney, and A. K. Roy, "Thermal properties of graphene: Fundamentals and applications," *MRS Bulletin*, vol. 37, no. 12, p. 1273–1281, 2012.
- [62] K. Kim, J. He, B. Ganeshan, and J. Liu, "Disorder enhanced thermal conductivity anisotropy in two-dimensional materials and van der waals heterostructures," *Journal of Applied Physics*, vol. 124, no. 5, p. 055104, 2018.
- [63] J. Liu, G.-M. Choi, and D. G. Cahill, "Measurement of the anisotropic thermal conductivity of molybdenum disulfide by the time-resolved magneto-optic kerr effect," *Journal of Applied Physics*, vol. 116, no. 23, p. 233107, 2014.
- [64] D. O. Lindroth and P. Erhart, "Thermal transport in van der waals solids from first-principles calculations," *Physical Review B*, vol. 94, no. 11, p. 115205, 2016.
- [65] K. M. Hoogeboom-Pot, J. N. Hernandez-Charpak, X. Gu, T. D. Frazer, E. H. Anderson, W. Chao, R. W. Falcone, R. Yang, M. M. Murnane, H. C. Kapteyn *et al.*, "A new regime of nanoscale thermal transport: Collective diffusion increases dissipation efficiency," *Proceedings of the National Academy of Sciences*, vol. 112, no. 16, pp. 4846–4851, 2015.
- [66] G. Barbalinardo, C. A. Sievers, S. Chen, and D. Donadio, "Thermal transport in finite-size van der waals materials: Modeling and simulations," in *2018 IEEE 18th International Conference on Nanotechnology (IEEE-NANO)*. IEEE, 2018, pp. 1–2.
- [67] A. Szabo, S. J. Koester, and M. Luisier, "Ab-initio simulation of van der Waals MoTe₂-SnS₂ heterotunneling FETs for low-power electronics," *IEEE Electron Device Letters*, vol. 36, no. 5, pp. 514–516, 2015.
- [68] X. Yan, C. Liu, C. Li, W. Bao, S. Ding, D. W. Zhang, and P. Zhou, "Tunable s_nse₂/wse₂ heterostructure tunneling field effect transistor," *Small*, vol. 13, no. 34, p. 1701478, 2017.
- [69] T. Roy, M. Tosun, X. Cao, H. Fang, D. Lien, P. Zhao, Y. Chen, Y. Chueh, J. Guo, and A. Javey, "Acs nano 2015, 9, 2071–2079."
- [70] M. Luisier, A. Schenk, W. Fichtner, and G. Klimeck, "Atomistic simulation of nanowires in the $sp^3d^5s^*$ tight-binding formalism: From boundary conditions to strain calculations," *Phys. Rev. B*, vol. 74, p. 205323, Nov 2006. [Online]. Available: <https://link.aps.org/doi/10.1103/PhysRevB.74.205323>
- [71] R. Rhyner and M. Luisier, "Phonon-limited low-field mobility in silicon: Quantum transport vs. linearized boltzmann transport equation," *Journal of Applied Physics*, vol. 114, no. 22, p. 223708, 2013. [Online]. Available: <https://doi.org/10.1063/1.4845515>
- [72] T. Markussen, A.-P. Jauho, and M. Brandbyge, "Electron and phonon transport in silicon nanowires: Atomistic approach to thermoelectric properties," *Phys. Rev. B*, vol. 79, p. 035415, Jan 2009. [Online]. Available: <https://link.aps.org/doi/10.1103/PhysRevB.79.035415>
- [73] J. He, K. Hummer, and C. Franchini, "Stacking effects on the electronic and optical properties of bilayer transition metal dichalcogenides mos₂, mose₂, ws₂, and wse₂," *Phys. Rev. B*, vol. 89, p. 075409, Feb 2014. [Online]. Available: <https://link.aps.org/doi/10.1103/PhysRevB.89.075409>
- [74] J. Shi, R. Tong, X. Zhou, Y. Gong, Z. Zhang, Q. Ji, Y. Zhang, Q. Fang, L. Gu, X. Wang *et al.*, "Temperature-mediated selective growth of mos₂/ws₂ and ws₂/mos₂ vertical stacks on au foils for direct photocatalytic applications," *Advanced Materials*, vol. 28, no. 48, pp. 10664–10672, 2016.
- [75] M. Chiu, M. Li, W. Zhang, W. Hsu, W. Chang, M. Terrones, H. Terrones, and L. Li, "Acs nano 2014, 8, 9649–9656."
- [76] J.-J. Ma, J.-J. Zheng, X.-L. Zhu, P.-F. Liu, W.-D. Li, and B.-T. Wang, "First-principles calculations of thermal transport properties in mos₂/mose₂ bilayer heterostructure," *Physical Chemistry Chemical Physics*, vol. 21, no. 20, pp. 10442–10448, 2019.
- [77] L. Yu, V. Ranjan, W. Lu, J. Bernholc, and M. B. Nardelli, "Equivalence of dipole correction and coulomb cutoff techniques in supercell calculations," *Phys. Rev. B*, vol. 77, p. 245102, Jun 2008. [Online]. Available: <https://link.aps.org/doi/10.1103/PhysRevB.77.245102>
- [78] S. Jiang, L. Greengard, and W. Bao, "Fast and accurate evaluation of nonlocal coulomb and dipole-dipole interactions via the nonuniform fft," 2013.
- [79] J. P. Perdew, K. Burke, and M. Ernzerhof, "Generalized gradient approximation made simple," *Phys. Rev. Lett.*, vol. 77, pp. 3865–3868, Oct 1996. [Online]. Available: <https://link.aps.org/doi/10.1103/PhysRevLett.77.3865>
- [80] S. Grimme, "Semiempirical gga-type density functional constructed with a long-range dispersion correction," *Journal of computational chemistry*, vol. 27, no. 15, pp. 1787–99, 2006.
- [81] G. Kresse and J. Furthmüller, "Efficient iterative schemes for *ab initio* total-energy calculations using a plane-wave basis set," *Phys. Rev. B*, vol. 54, no. 16, pp. 11169–11186, October 1996. [Online]. Available: <http://link.aps.org/doi/10.1103/PhysRevB.54.11169>
- [82] G. Kresse and J. Furthmüller, "Efficiency of ab-initio total energy calculations for metals and semiconductors using a plane-wave basis set," *Computational Materials Science*, vol. 6, no. 1, pp. 15 – 50, 1996. [Online]. Available: <http://www.sciencedirect.com/science/article/pii/S0927025696000080>
- [83] A. Togo and I. Tanaka, "First principles phonon calculations in materials science," *Scr. Mater.*, vol. 108, pp. 1–5, Nov 2015.
- [84] N. O. Weiss, Y. Huang, Y. Liu, X. Duan, X. Duan, and H.-C. Cheng, "Van der waals heterostructures and devices," *Nature Reviews Materials*, 2016.
- [85] E. Gnani, A. Gnudi, S. Reggiani, M. Luisier, and G. Bacarani, "Band effects on the transport characteristics of ultrascaled snw-fets," *IEEE Transactions on Nanotechnology*, vol. 7, no. 6, pp. 700–709, 2008.

- [86] K. Kölbig and B. Schorr, "A program package for the landau distribution," *Computer Physics Communications*, vol. 31, no. 1, pp. 97 – 111, 1984. [Online]. Available: <http://www.sciencedirect.com/science/article/pii/0010465584900857>
- [87] T. D. Kühne, M. Iannuzzi, M. Del Ben, V. V. Rybkin, P. Seewald, F. Stein, T. Laino, R. Z. Khaliullin, O. Schütt, F. Schiffmann *et al.*, "Cp2k: An electronic structure and molecular dynamics software package-quickstep: Efficient and accurate electronic structure calculations," *The Journal of Chemical Physics*, vol. 152, no. 19, p. 194103, 2020.